CrossMark

Electromagnetic and Rotational Characteristics of a Superconducting Flywheel Energy Storage System Utilizing a Radial-Type High-Temperature Superconducting Bearing

Zhiqiang Yu[1] · GuoMin Zhang[2] · Qingquan Qiu[2] · Dong Zhang[2] · Xiaoyun Sun[1] · Shuohe Wang[1] · Yuzhi Liu[1] · Wenjie Feng[1] · Wanjie Li[2] · Liwang Ai[2]

Abstract

A 2 kW/28.5 kJ superconducting flywheel energy storage system (SFESS) with a radial-type high-temperature superconducting (HTS) bearing was set up to study the electromagnetic and rotational characteristics. The structure of the SFESS as well as the design of its main parts was reported. A mathematical model based on the finite element method (FEM) was established to research the electromagnetic characteristics of the HTS bearing during the levitation process, which show that a part of the magnetic flux penetrates into the edge of the HTS bulks and then goes back to the opposite pole of the permanent magnet rotor (PMR). The induced current mainly distributes in the edge of the HTS bulks, indicating that larger force acts on the edge part of the HTS bulks and probably causes them to crack. The free rotations of the rotor at different steady-state speeds of 2500–5000 rpm and its radial vibration were displayed. The induced voltage of the stator winding of the motor in this process was analyzed. The rotational characteristics are related to the vibration of the rotor. Below the resonant frequency, the vibration increases significantly with the speed. Enhancing the radial stiffness to limit the vibration amplitude of the rotor is an effective approach to improve the speed.

Keywords Bulk superconductivity · Devices · Bulk magnetism

1 Introduction

High-temperature superconductors have many good properties, of which diamagnetic and flux pinning properties can be used to achieve passive and stable levitation in combination with permanent magnets (PMs) [1]. These properties make them attractive for use in engineering applications. Among them, superconducting flywheel energy storage systems (SFESSs) [2–5] and Maglev transportations [4, 6] are regarded as ones of the most promising equipment. For a SFESS with a high-temperature superconducting (HTS) bearing, it has greater advantages and potential applications

in many fields such as wind power, solar power and power system [2, 7].

In the past decade, many SFESSs have been successfully developed. The Boeing group (USA) designed a 5 kWh/100 kW SFESS in 2007. Based on this system, they further manufactured a 5 kWh/3 kW SFESS in 2009 [3]. The two SFESSs used the axial-type HTS bearings with the same structure and their loss was studied. ATZ (Germany), in 2007, fabricated a compact 5 kWh/250 kW SFESS with a radial-type HTS bearing [4]. They investigated the structure of the radial-type HTS bearing in detail. The rotor of the SFESS they developed weighed 450 kg. In 2006, ISTEC (Japan) constructed a 10 kWh/100 kW SFESS, with a radial-type HTS bearing (outer-rotor type) and two active magnet bearings (AMBs) [8]. They improved the cooling structure of the HTS bearing and studied the loss of the AMBs and the overall loss. KEPRI (Korea) developed a 35 kWh SFESS with two hybrid bearing sets (each one includes an HTS bearing and an active magnetic damper) in 2012 [9]. Compared with their previously designed SFESSs, the stiffness

✉ GuoMin Zhang
  gmzhang@mail.iee.ac.cn

[1] Shijiazhuang Tiedao University, Shijiazhuang 050043, China

[2] Institute of Electrical Engineering, Chinese Academy of Sciences, Beijing 100190, China

of the new system has been greatly increased. It has been used for the electric power stability of subway stations. In 2016, Furukawa Electric Corporation (Japan) developed a 300 kW SFESS [5]. In this system, the stator and rotor of the HTS bearing are both made of superconducting materials (the stator is winded using rare-earth $Ba_2Cu_3O_y$ tape, and the rotor is a disc made of $YBa_2Cu_3O_y$). It can levitate 4-ton rotor. Up to now, the system has been applied in the railway power grid. Besides, recently to reduce the hysteresis losses, ULisboa (Portuguese) performed static tests on a SFESS with a radial-type HTS bearing in zero-field cooling [10]. SBU (Iran) cooperating with UH (USA) used the disc-shaped bulks to make the superconductor magnet stator (SMS) and optimized its structure [11]. IUST (Iran) theoretically analyzed the sensitivity of the rotor parameters [12]. UFRJ (Brazil) and GTU (Turkey) also have been working on the related research [13, 14].

In 2001, IEE CAS (China) firstly set up a small SFESS with an axial-type HTS bearing and two AMBs in China [15]. Recently we have done some works on the radial-type HTS bearing for the SFESS, including studying the magnetic field characteristics of the PM rotor (PMR), optimizing the structure [16] and analyzing the levitation characteristics using the finite element method (FEM) [17]. Based on these works, we built a small-power SFESS with a radial-type HTS bearing and an external motor. The electromagnetic characteristics and rotation of the SFESS were researched and discussed in this paper. It is organized as follows: Section 2 describes the structure and main parts of the SFESS in detail. Section 3 shows the measurement process and results of the levitation force. A mathematical model was set up to study the electromagnetic characteristics and current density distribution in the HTS bulks during the levitation process. The free rotations with different steady-state speeds were displayed, and the reasons for the speed decay were taken fully into account. The rotational characteristics were analyzed.

Finally, Section 4 draws the main conclusions of this work. The small SFESS built in this paper provides an important basis for the development of a large-scale system.
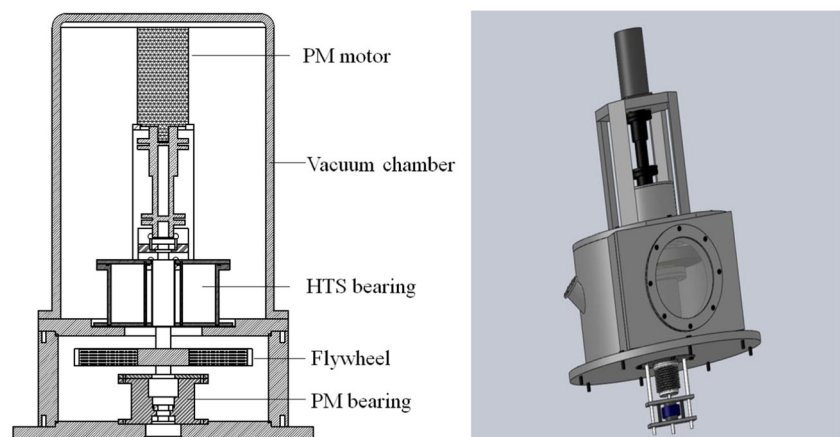
2 SFESS Design

The structure of the SFESS is shown in Fig. 1. The major components include a 3-kg flywheel that utilizes reinforced composites, a 2-kW brushless PM motor that drives the flywheel to spin, a radial-type HTS bearing that levitates the rotor and suppresses its radial vibration, two pedestals that protect the rotor from damage both radially and axially, and a vacuum chamber that provides a vacuum environment. The design parameters of the SFESS are given in Table 1. The whole system was fixed on the support platform with the bolts. The flywheel body as well as the PMR of the HTS bearing was fitted on the shaft (together called the rotor). When assembling the PMR, the same poles of PM rings faced each other so that there was a great repulsion. Thus we used the fixture to clamp and then glued them. The motor was supported by a bracket fixed to the cover plate of the flywheel-running cavity. When the SFESS stopped working, the rotor was hold up by the thrust protection bearing at the bottom of the shaft.

2.1 Flywheel Body

A flywheel, one of the most important components in the SFESS, is used to store the mechanical energy. The amount of energy stored in a flywheel is proportional to the moment of inertia and the square of rotational speed. For the established SFESS, the flywheel body is mounted on the shaft together with the PMR of the HTS bearing and that of the PM bearing, consisting of glass fiber, carbon fiber-reinforced composites and an aluminum alloy hub, as

Fig. 1 Structure of the SFESS and its 3D model

Table 1 Design parameters of SFESS

Design parameters	Value or characteristics
Capacity	28.5 kJ/2 kW
Rated speed	10,000 rpm
Type of HTS bearings	Radial-type (inner-rotor type)
Flywheel weight	3 kg
Weight of rotor	9.8 kg
Height of rotor	363 mm
Cooling method	Soaking with LN$_2$/conduction cooling
Overall size of SFESS	Φ510 mm×875 mm
Specific energy	0.81 Wh/kg
Power density	204.08 W/kg

shown in Fig. 2. It weighs 3 kg with the outer radius of 160 mm and inner radius of 20 mm. Its moment of inertia (J) and designed speed are 0.052 kg·m^2 and 20,000 rpm, respectively. When the speed of the rotor is 10,000 rpm (the rated speed), the maximum angular acceleration is 19.23 rad/s^2, and the maximum linear rim acceleration is 3.07 m/s^2 according to the formula $a = d\Omega/dt \cdot r$.

The stress distribution refers to the magnitude and direction of stress on the surface and internal points of an object under loading. It is related not only to the material and geometry of the object but also to the magnitude of load and loading method. At the designed speed (20,000 rpm), the stress distributions (including the radial stress, radial displacement and circumferential stress distribution) of the flywheel body are shown in Fig. 3. A comparison of the calculated and designed parameters of the flywheel is listed in Table 2. It indicates that the calculated parameters meet the design requirements completely.

2.2 HTS Bearing

For the designed SFESS, the HTS bearing, the key component to ensure the flywheel runs smoothly, is a radial-type bearing. We have done the related works on its structural

design and optimization [16, 17]. It mainly includes a PMR and a SMS surrounding the rotor (inner-rotor type).

The PMR is located near the upper of a nonmagnetic shaft, consisting of six axially polarized PM rings (NdFeB) separated by seven iron shims (1J22). The iron shims change the flux in the radial direction so that it will have a high gradient within the adjacent HTS bulks (YBCO). Each PM ring has an outer diameter of 36 mm, an inner diameter of 20 mm and a height of 8 mm. The iron shim has the same outer and inner diameters as those of the PM ring with the thickness of 2 mm. The magnetic flux density (B_r) at the outside surface of the iron shim between two neighboring PM rings is 0.85 T.

The SMS has an outer diameter of 200 mm, an inner diameter of 40 mm and a height of 160 mm. It is mainly made of the HTS bulks, cryogenic container and inner wall. There are three layers of bulks used in it (see Fig. 4). Each layer is composed of eight bulks (called one HTS ring), glued on the inner wall around the PMR (by using a low-temperature epoxy adhesive). The size of every HTS bulk is the dimension of 28 mm × 16 mm × 13 mm and then it was processed into a sector [18]. To fix the positions of the HTS bulks along axial direction, the bottom and middle pallets are designed and produced using epoxy resin. The bottom pallet is set on the bottom of the cryogenic container. The middle pallet is put between every two adjacent layers of the HTS bulks. There are 12 flutes on the bottom pallet and double flutes on every middle pallet so that the HTS bulks can be effectively cooled down by LN$_2$. Made of 304 stainless steel, the cryogenic container can store LN$_2$ and reduce heat losses. The LN$_2$ system for cooling the HTS bulks is a closed-loop system.

2.3 PM Motor

The transformation between rotational kinetic energy and electrical energy is performed with a 2-kW brushless PM motor. Main features of the motor are convenient control, wider speed range, high-power capability and high efficiency

Fig. 2 Structure of the flywheel body and photograph of the rotor (unit: mm, HTSB represents the HTS bearing, PMB represents the PM bearing)

a

b

c
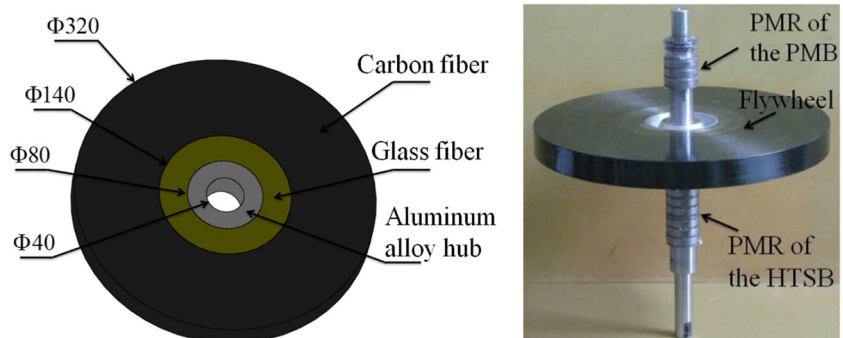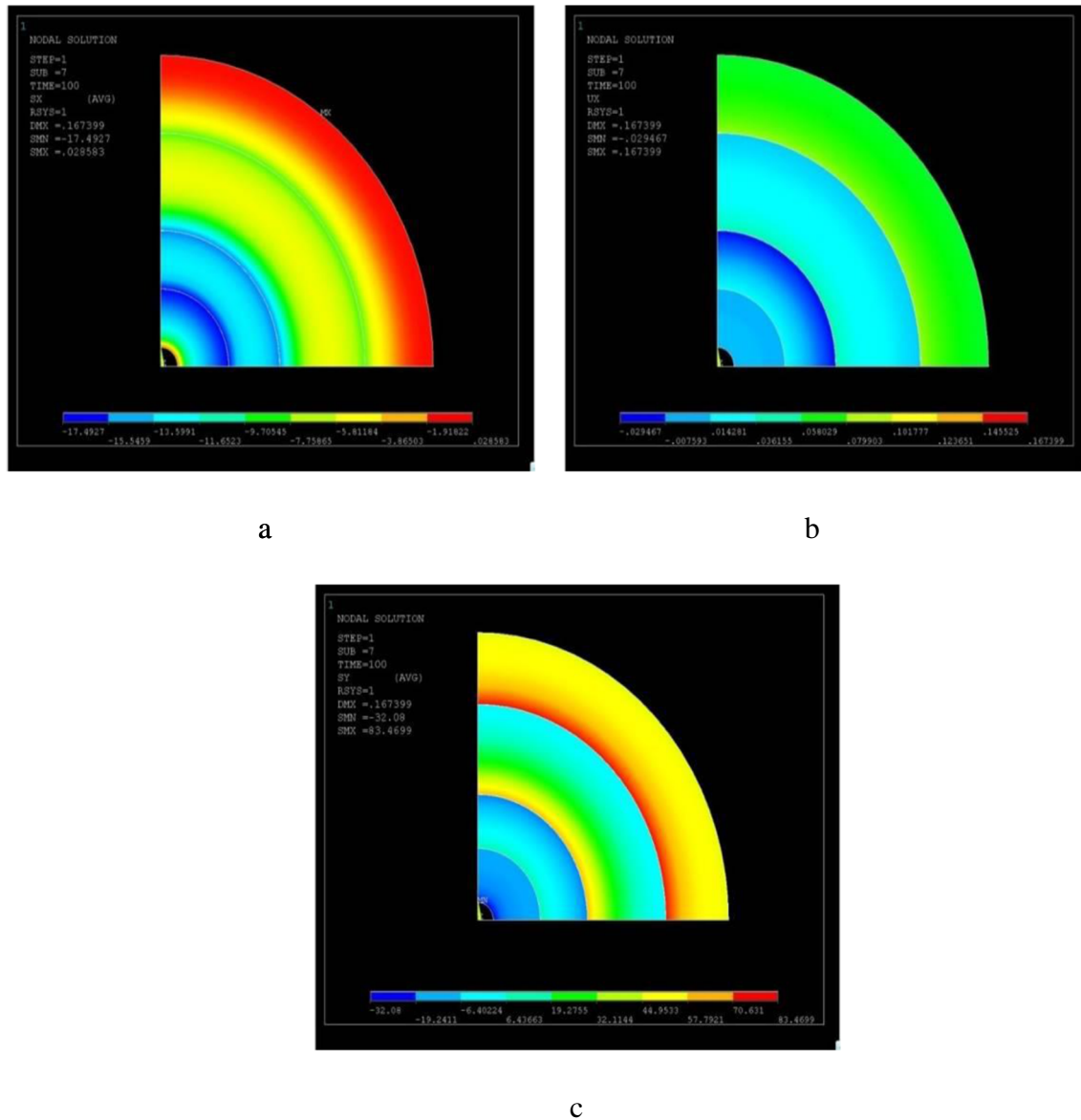
Fig. 3 Stress distributions of the flywheel body at 20,000 rpm **a** Its radial stress, **b** radial displacement and **c** circumferential stress distribution

both in motor and generator operation. The motor with the size of 92 mm × 92 mm × 175 mm has five poles. Its rated speed and torque are 10,000 rpm and 2 Nm, respectively.

The insulated gate bipolar transistor (IGBT) and microprocessor technology allow a reliable and efficient control over the speed and power range of the motor.

3 Results and Discussion

3.1 Levitation Force Measurement

The process of measuring the levitation force is shown in Fig. 5a. The PMR employed in the experiment consisted of

Table 2 Comparison of the calculated and designed parameters of flywheel

Parameters	Calculated values	Designed values
Radial deformation of outer diameter (mm)	0.07	–
Maximum circumferential tensile stress (MPa)	83.5	1600
Maximum circumferential compressive stress (MPa)	32.08	900
Maximum radial tensile stress (MPa)	0.03	19
Maximum radial compressive stress (MPa)	17.5	80

Fig. 4 Bonding and fixing of HTS bulks and photograph of the SMS. The diagram on the left is a 3D rendering showing the structure of the middle and bottom pallets. These pallets are all used in the SMS
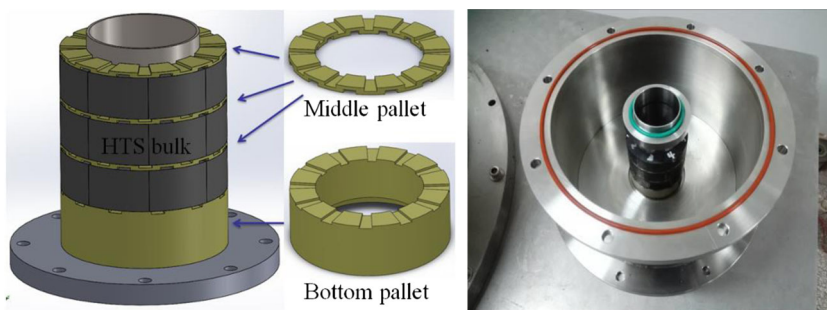
three PM rings and four iron shims. The PM rings as well as the iron shims had the same dimension to them of the PMR used in the SFESS. The magnetic field in the surface of the iron shims was also 0.85 T. The SMS was cooled by LN$_2$ for 35 min. The PMR moved along axial direction from 0 to 10 mm and then back to 0 mm. The measured results show that the maximum levitation force is 100 N greater than the rotor weight (see Fig. 5b). Moreover, when we did the experiments using the six-PM ring PMR of the SFESS, the levitation stiffness reaches to 53 N/mm. So the HTS bearing can fully levitate the rotor of the SFESS.

3.2 Levitation and Electromagnetic Characteristics

3.2.1 Mathematical Model

In field cooling, the levitation force belonging to an electromagnetic force is mainly from the pinning force of the HTS bulks. From a microscopic point of view, the pinning force density depends on both the number density of pinning centers and elementary pinning force. Given superconducting materials and an external magnetic field, the two factors

are approximately constant. Regarding the levitation process of the HTS bearing, the external magnetic field is varied owing to the moving of the PMR. Thus the pinning force density is not constant so that the levitation force is a variable. From the macroscopic point of view, the levitation force is the electromagnetic force due to the induced current of superconductors in the external magnetic field, expressed by the equation $F = \int J \times B dV$. Currently, main methods of calculating the electromagnetic force are the FEMs [19–22]. Compared with AV [19] and $T\Omega$ formulation [20], H formulation has the advantages in the computation complexity and simplification equations, etc. [21, 22]. So based on H formulation we set up the mathematical model to analyze the electromagnetic characteristics. Figure 6a shows the diagram of the model in a 2D axisymmetric space. The process of the model building is briefly described as follows: according to Maxwell's equations, we can obtain the governing equation for the whole calculation domain (S)

$$\mu \frac{\partial H}{\partial t} + \nabla \times (\rho \nabla \times H) = 0 \tag{1}$$

Fig. 5 Measurement of the levitation force. **a** The experimental process and **b** results

a

b
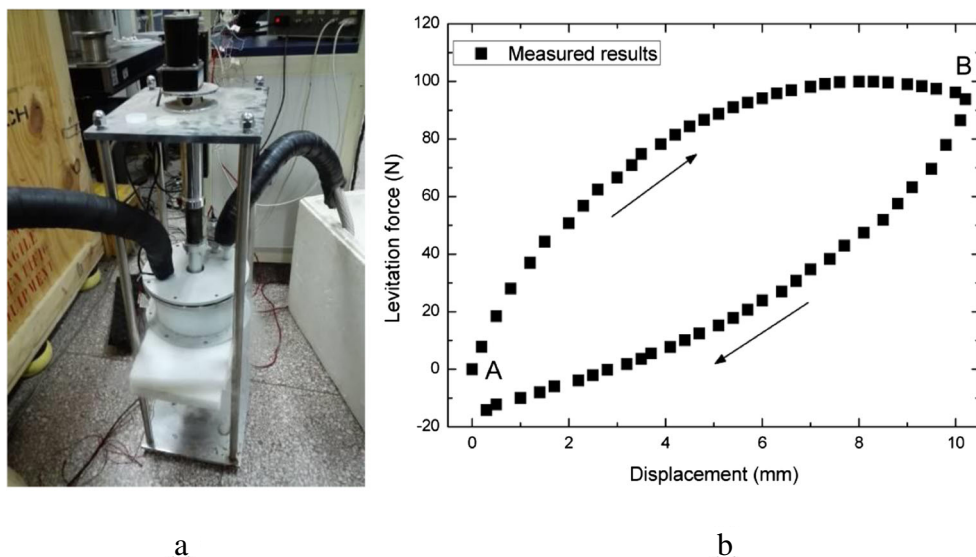
Fig. 6 Numerical calculation. **a** The diagram of the mathematical model and **b** calculated results (PM represents one PM ring, Mov. represents the moving direction of the PMR, and the iron shim locates between the two adjacent PMs or on the top and bottom of the PMR)

a

b
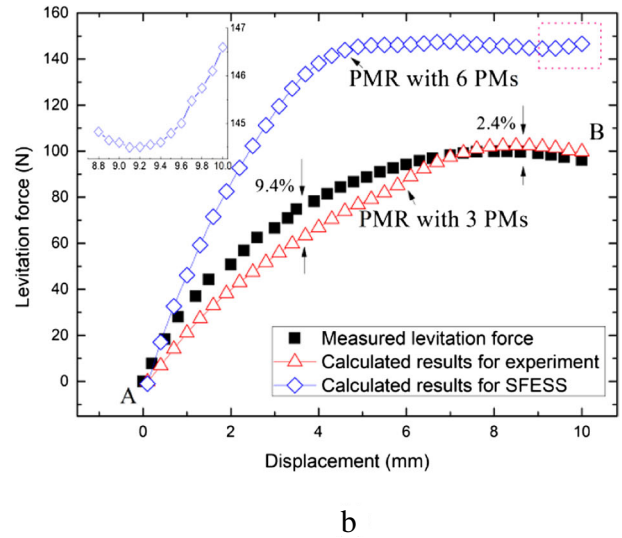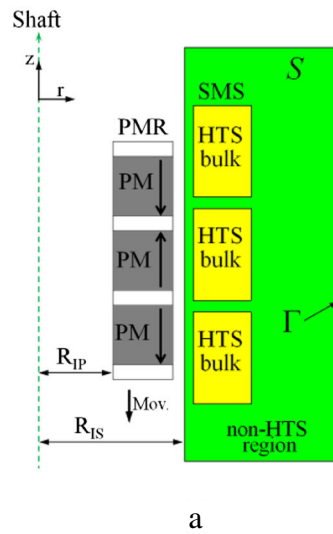
Based on Galerkin's method and Green's formula, the weak form of (1) can be obtained

$$\int_S \mu \frac{\partial H}{\partial t} \cdot W dS - \rho \int_S \frac{1}{r} \frac{\partial H}{\partial r} \cdot W dS + \rho \int_S \frac{\partial H}{\partial r} \cdot \frac{\partial W}{\partial r} dS$$
$$+ \rho \int_S \frac{\partial H}{\partial z} \cdot \frac{\partial W}{\partial z} dS - \rho \int_\Gamma \frac{1}{r} \frac{\partial H}{\partial n} \cdot W d\Gamma = 0 \quad (2)$$

Selecting the interpolation function N_j, e.g., first-order triangular element, we can write the expression of vector H in one element, i.e, $H = H_j^e(t) N_j$, $j = 1, 2, 3$. According to Galerkin's method weight function $(W) = N_i$, $i = 1, 2, 3$, where i and j are the local numbers of nodes of element. Thus, we can write the equation of one node of the element by (2)

$$\int_{S^e} \mu \frac{dH_j^e(t) N_j}{dt} N_i dS^e - \rho \int_{S^e} \frac{1}{r} \frac{\partial N_j}{\partial r} N_i H_j^e(t) dS^e$$
$$+ \rho \int_{S^e} \frac{\partial N_j}{\partial r} \cdot \frac{\partial N_i}{\partial r} H_j^e(t) dS^e$$
$$+ \rho \int_{S^e} \frac{\partial N_j}{\partial z} \cdot \frac{\partial N_i}{\partial z} H_j^e(t) dS^e$$
$$- \rho \int_\Gamma^e \frac{1}{r} \frac{\partial N_j}{\partial n} N_i H_j^e(t) d\Gamma^e = 0 \quad (3)$$

If setting $M_{ij}^e(\mu) = \int_{S^e} \mu N_j N_i dS^e$ and

$$S_{ij}^e(\rho) = \rho \int_{S^e} \left[-\frac{1}{r} \frac{\partial N_j}{\partial r} N_i + \frac{\partial N_j}{\partial r} \cdot \frac{\partial N_i}{\partial r} + \frac{\partial N_j}{\partial z} \cdot \frac{\partial N_i}{\partial z} \right] dS^e$$
$$- \rho \int_{\Gamma^e} \frac{1}{r} \frac{\partial N_j}{\partial n} N_i d\Gamma^e,$$

Equation (3) can be expressed as

$$M_{ij}^e(\mu) \frac{dH_j^e(t)}{dt} + S_{ij}^e(\rho) H_j^e(t) = 0 \quad (4)$$

Hence, the equations of all the nodes of the element are accumulated to obtain a matrix form

$$[M^e(\mu)] \frac{d}{dt} \{H^e(t)\} + [S^e(\rho)]\{H^e(t)\} = 0 \quad (5)$$

where the superscript e denotes the value of parameters at each element meshed by FEM technique, $[M^e(\mu)]$ is the element mass matrix, $[S^e(\rho)]$ is the element stiffness matrix and $\{H^e(t)\}$ is the element column vector. In the temporal domain by the finite difference technique via a backward Euler's method, the final equation of the nonlinear system to be numerically solved takes the following form:

$$([\mathbf{M}(\mu)] + [\mathbf{S}(\rho)] \cdot \Delta t) \{\mathbf{H}^n\} = [\mathbf{M}(\mu)] \{\mathbf{H}^{n-1}\} \quad (6)$$

where Δt is the time interval between the successive time instants and the superscript n and $n - 1$ represent the column vector for the current time instant and the last time instant, respectively. The mass matrix $[\mathbf{M}(\mu)]$ as well as the stiffness matrix $[\mathbf{S}(\rho)]$ is formed by the superposition of all element matrixes. The vector $\{\mathbf{H}^{n-1}\}$ is known at each time instant and provides the source term. The successive overrelaxation (SOR) method was used to solve the linear equations. The relaxation factor was taken between 0 and 1. The iteration could be terminated if the relative error is less than a given standard value. When the time step reaches its maximum, the calculation is complete. Then, the current density and magnetic field strength of all nodes in S are obtained. So, the levitation force, in a 2D axisymmetric space, can be calculated by

$$F = 2\pi \int_S r J_{sc} B_r dS = 2\pi \sum_{i=1}^{Ng} \sum_{j=1}^{Mk} r_i^e J_{sc,j,i}^e B_{r,j,i}^e \Delta S_{sc,j,i}^e \quad (7)$$

where ΔS_{sc}^e represents the area of each element in superconducting subdomain, M_k is the amount of the node of its each

element, N_g is the number of its mesh element, J_{sc}^e indicates the critical current at the node of the element (calculated according to Ampere's law: $J = \partial H_r/\partial z - \partial H_z/\partial r$), and B_r^e is the radial component of the magnetic field at the node of the element. The mathematical model was successfully implemented using a FORTRAN code generated by the FEPG software.

3.2.2 Electromagnetic Characteristics

With the above proposed model, we calculated the levitation force (A-B section corresponding to the displacements of 0–10 mm) and compared it with the measured result, shown in Fig. 6b. The calculation parameters are indicated in Table 3, including critical current density (J_c), effective resistivity (ρ_{sc}), prescribed tolerance (ε), E_c and exponent n (defined as U/kT) of the EJ model, velocity of the PMR (v), magnetization M of the PM ring, and number (n_e) of the mesh element. The LN$_2$ temperature is 77 K in the calculation and the Kim model is considered [17]. From Fig. 6b, the calculated results match well the measured, with a maximum relative discrepancy of 9.4% in the rise section (corresponding to the displacements of 0–5 mm) and 2.4% in the saturation section (corresponding to the displacements of 5–10 mm). The shape and trend of the calculation curve generally agree with those in Basaran and Sivrioglu [14] and Yu et al. [16]. The discrepancies may be attributed to the following reasons: for one thing, in the experiment, during the field cooling or the moving of the PMR, the z-axis of the PMR does not completely coincide with that of the SMS. For another, the position of the PMR in field cooling is not at the geometric center of the SMS. In addition, for the FEM calculation, the uncertainty of parameter values also affects the fit. For example, if J_{c0} is set to more precise value, i.e., its significant digits are increased after the decimal point, the discrepancies could become less, and the discrepancies could also become less. For n and initial effective resistivity (ρ_{sc}), within their ranges, they have trivial effect on the discrepancies as well.

We showed the calculated levitation-force curve for the SFESS in Fig. 6b, the PMR of the HTS bearing in the system including six PM rings. The maximum of the levitation force is 150 N, 50 N higher than that of the measured with the PMR consisting of three PM rings. During the PMR moving to 9–10 mm, its five magnetic poles are close to the middle positions of the HTS bulks in the z-direction. So the amount of pinned magnetic flux continues to increase, resulting in an increase of induced current density (J_{sc}) and

then the levitation force (see the inset of Fig. 6b). From the curve shape of the SFESS, its saturation section is flatter, indicating that the saturation of the magnetic flux is much higher. Besides, this also shows that the levitation force can be increased with a stronger external magnetic field. But this method of increasing the levitation force is limited due to the saturation property of the pinning force density in II-type superconductors.

Figure 7 depicts the magnetic field (H) and distributions of J_{sc} in HTS bulks of the SMS during the levitation process. There are substantial magnetic field lines gathering at the positions of the iron shims (Fig. 7a). A part of the magnetic flux penetrates into the edge of the HTS bulks and then goes back to the opposite pole near the next iron shim. There is seldom flux going through the HTS bulks along r-direction. As a result, a great deal of the magnetic field lines is confined in two kinds of small gaps: one is between the PMR and SMS (in the r-direction), and the other is between every two adjacent HTS bulks (in the z-direction). From the perspective of 2D space, the distributions of J_{sc} are similar to those of H entering to the HTS bulks. Moreover, note that the distributions of J_{sc} are mainly on the edges of the HTS bulks so that there is larger force on there (Fig. 7b), which is one of the reasons that this part is prone to the crack during the operation of the SFESS. The effect on the outer-rotor-type HTS bearing could be greater. From Fig. 7b, the value and summation of J_{sc} corresponding to the displacement of 6 mm, 8 mm and 10 mm are larger, showing that there is larger levitation force at these positions. This agrees with the measured and calculated results.

3.3 Rotational Characteristics of Rotor

When the rotor of the SFESS rotates freely, the PM motor runs as a generator (i.e. a load) and its stator windings will generate an induced voltage. Due to the load torque and rotational losses, the speed decreases continuously, with which the amplitude and frequency of the induced voltage simultaneously change. Below, we discuss these characteristics. A comparison of the free rotations with different steady-state speeds is shown in Fig. 8. The inset of Fig. 8a indicates the decelerations of the speeds. Generally the higher the steady-state speed, the greater the deceleration. The speed decay process can be divided into three phases (respectively called the beginning, middle and end phases) according to the deceleration. In the beginning phase, the slope of the deceleration is the greatest and then gradually becomes small. It overall becomes smaller

Table 3 Calculation parameters

J_{c0} (A/m^2)	ρ_{sc} (Ω/m)	ε (A/m)	E_c (V/m)	n (U/kT)	v (m/s)	M (kA/m)	n_e
6.5×10^7	1×10^{-16}	1×10^{-3}	1×10^{-4}	15	1×10^{-3}	836	1369
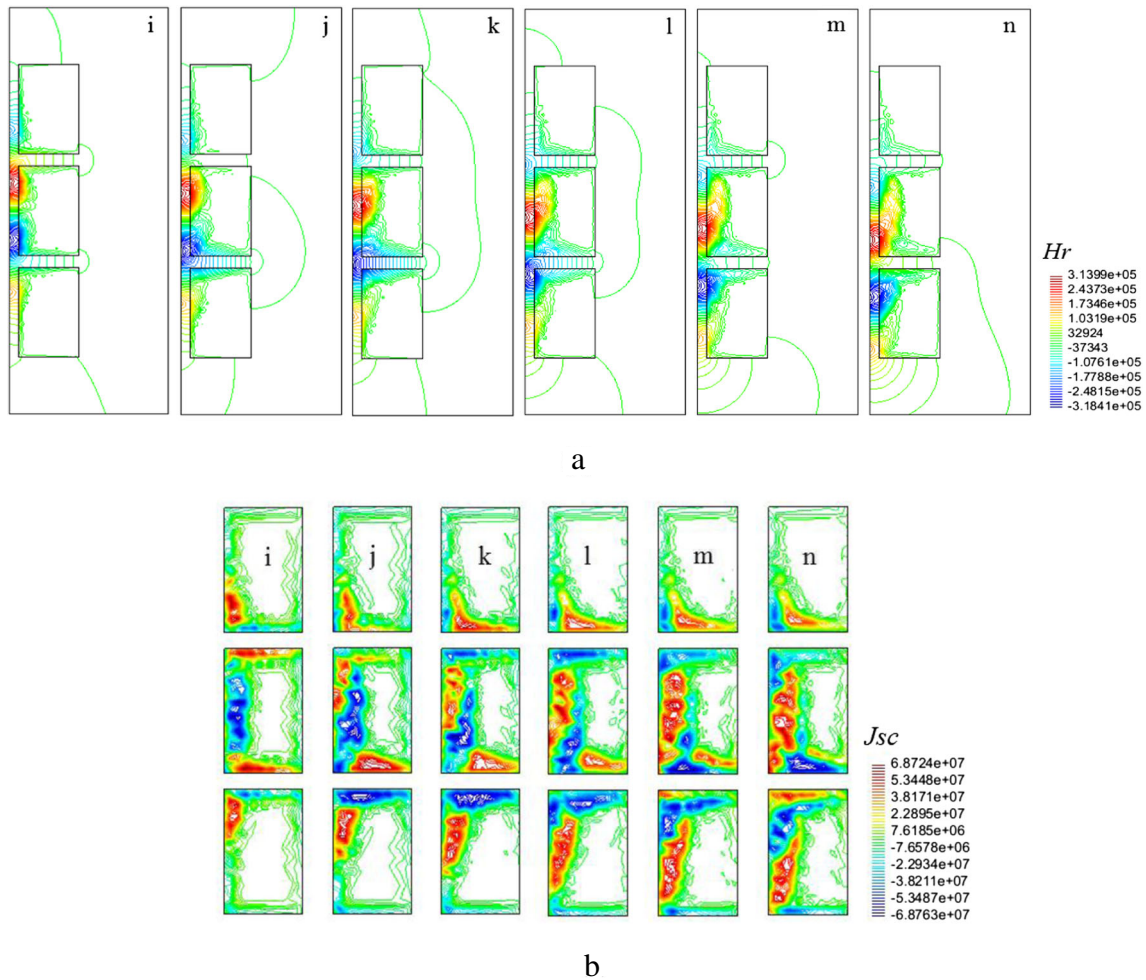
Fig. 7 Electromagnetic behavior of the HTS bearing in the SFESS during the levitation process. **a** Change of radial component (H_r) of magnetic field and **b** distributions of J_{sc} in HTS bulks for six displacements from 0 to 10 mm (i, j, k, l, m and n represents the PMR's displacement of 0 mm, 2 mm, 4 mm, 6 mm, 8 mm and 10 mm, respectively)

in the middle. While in the end phase, the speed decay becomes very slower and the deceleration is relatively flat. For example, considering the steady-state speed of 5000 rpm, in the first 40 s (the beginning phase), the speed is reduced to about half of the steady-state speed and the average deceleration is −123.5 rpm/s; after 40 s (the middle phase), the speed decay is gradually slowed down and the average deceleration is −61.4 rpm/s. At 80 s, the speed is reduced by about a quarter of the steady-state speed. When in the end phase, especially in the last 10 s, the value of the speed decay is only 69 rpm and the average deceleration is −14.7 rpm/s.

To study the variation of the induced voltage (u_d) of the motor stator windings with the free rotations of the rotor (i.e., speed decay), a comparison of u_d in 0.1 s respectively during the beginning, middle and end phases when the steady-state speed is 3000 rpm is shown in Fig. 8b. For 0.1 s in the beginning phase (0 s to 0.1 s), the average amplitude and frequency of u_d are the largest of the three phases. The

maximum amplitude is 32.29 V and the average frequency is 85 Hz For 0.1 s in the middle phase (40 s to 40.1 s) when the speed drops to 1350 rpm the maximum amplitude of u_d is 1492 V and its average frequency is 25 Hz. In the end phase, when the speed drops to 206 rpm the amplitude and frequency become very small (see the inset of Fig. 8b), with the maximum amplitude of 2.06 V and the average frequency of 3.84 Hz.

We normalize and compare the above data. The trend of the normalized amplitude and frequency of u_d and the speed for the three phases is depicted in Fig. 8c. The rates of the decrease of the amplitude and frequency of u_d and that of the speed are almost the same from the beginning to middle phase. They all drop to about 28%, the largest decreases in the speed being 26.4%. From the middle to end phase, the difference among the three gradually increases, in which the reduction of the frequency of u_d is the fastest and about 25% while the amplitude is the slowest and about 18%. Generally, the rates of decrease of the three

a

b

c
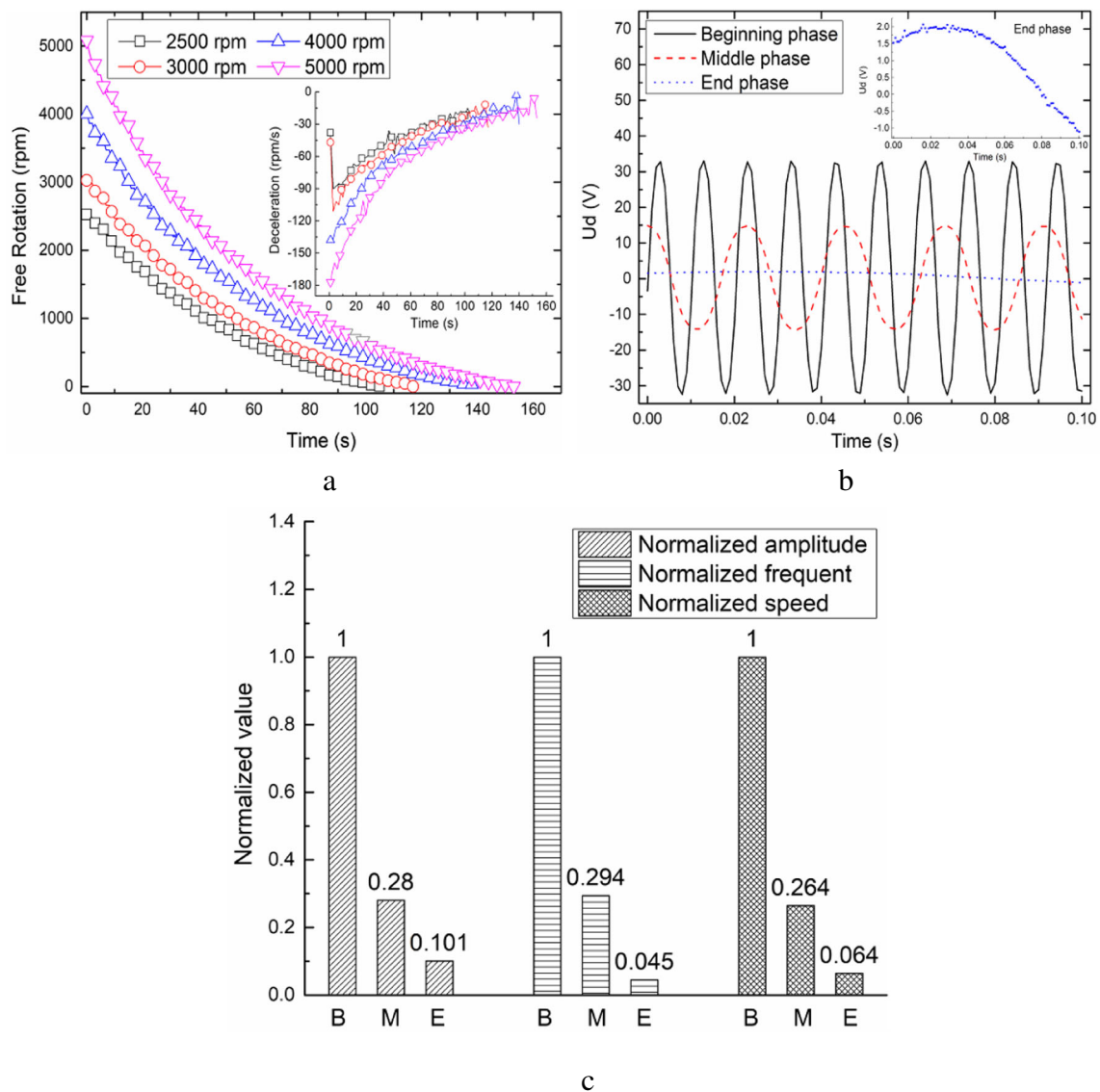
Fig. 8 Free rotations with different steady-state speeds. **a** The free rotations with 2500–5000 rpm. **b** A comparison of the induced voltages of the motor (u_d) in three phases with the steady-state speed of 3000 rpm. **c** A comparison of the normalized amplitude and frequency of the induced voltage and the speed (B represents the beginning phase, and M and E represent the middle and end phases, respectively)

Fig. 9 Operation of the SFESS. **a** The SMS in field cooling and **b** its discharge (the loads are four 16-W spotlights)


a

b
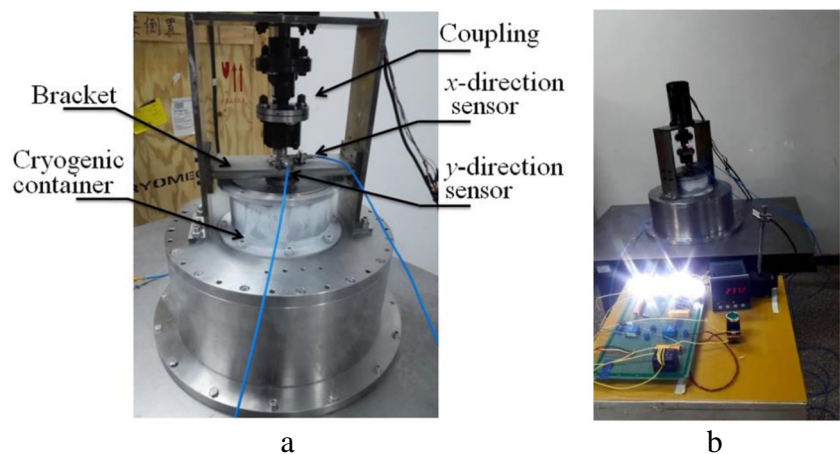
parameters from the middle to end phase are much less than those from the beginning to middle phase. We think that this is directly related to the reduction in vibration of the rotor due to the decreasing of the speed. That is, the vibration is proportional to the speed. When the vibration decreases, the rotor rotates more smoothly. As the average amplitude of induced voltage is the highest and the output power is the greatest in the beginning phase, it is the first-choice phase for the SFESS discharge. So extending the beginning phase is important for improving the SFESS performance.

For the SFESS, the loss due to the rotation of the rotor mainly comes from the following aspects: (a) the eddy current losses and hysteresis losses in the armature and casing produced by the rotor of the motor, (b) the eddy current losses of the stainless steel inner wall and the dewar of the SMS, (c) the eddy current losses of the iron shims, and (d) the hysteresis losses and eddy current losses of the HTS bulks generated by the PMR. To reduce the rotation losses, for the first one (a), we can use new materials or improve production process to reduce it, such as employing thin sheets made of noncrystalline material to manufacture the armature core of the PM motor. For (b) and (d), for example, reducing the cooling temperature for HTS bulks (supercooling) or using the HTS bulks with similar physical properties could decrease the losses effectively.
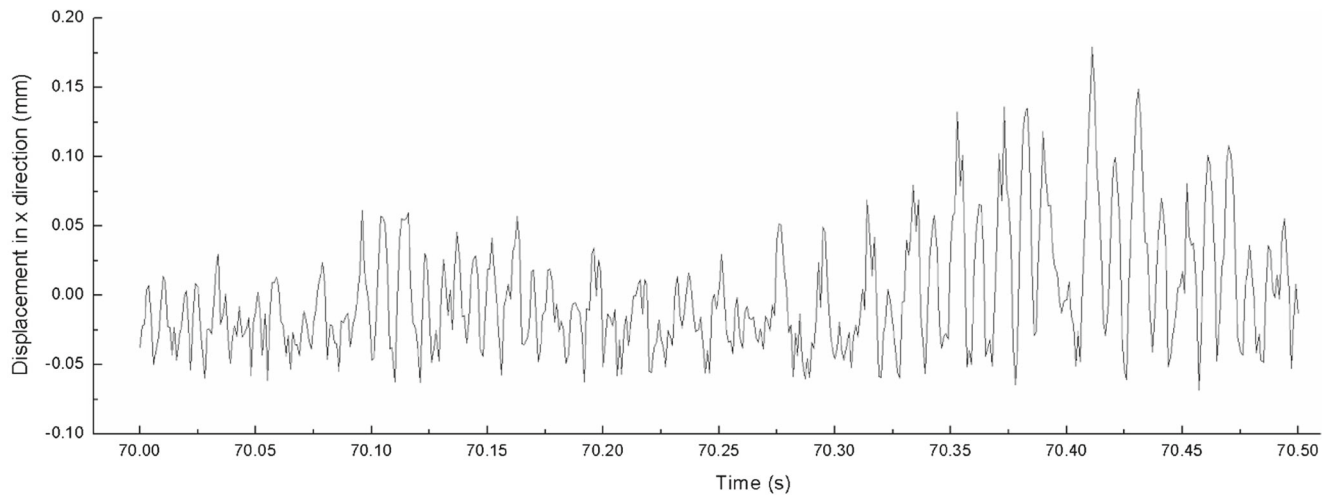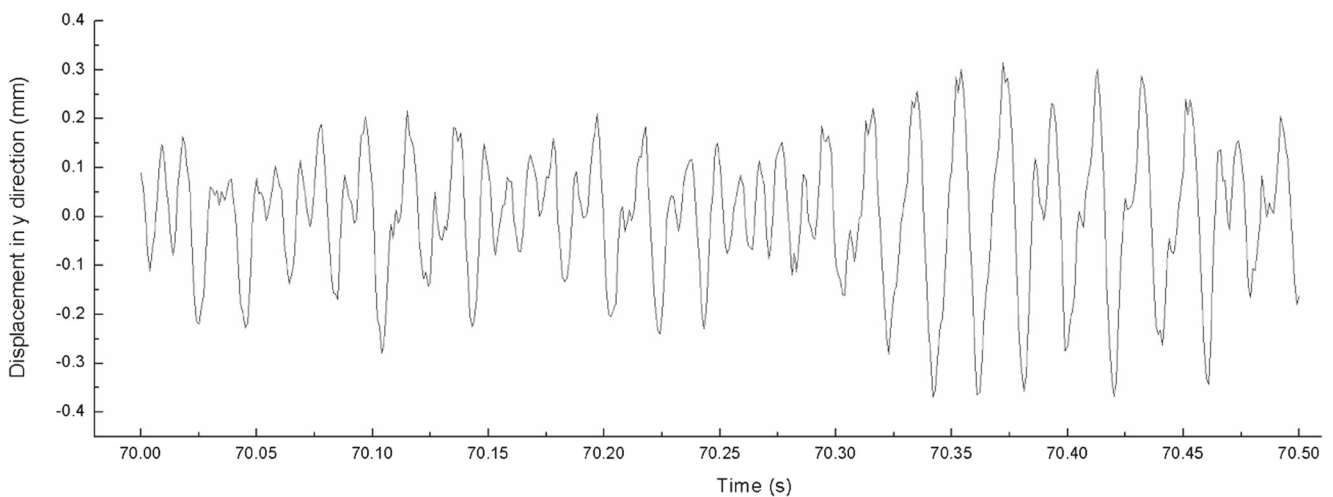
Fig. 10 Radial displacement of the rotor at the steady-state speed of 3000 rpm in the **a** x-direction and **b** y-direction

3.4 Radial Vibration of Rotor

The radial vibration of the rotor was detected by two eddy current sensors (called x- and y-direction sensor respectively, as shown in Fig. 9a). They were placed at 90° to each other. The probes of the sensors were mounted on the bracket below the coupling. The cable was connected to the corresponding pre-device. It converted the measurement signal to the corresponding voltage signal with a range of 0–5 V, which was ultimately sent to the computer.

Due to flexible connection between the rotor and motor shaft via the coupling, the rotor can move in 4 degrees of freedom. Since the constraint depends on the axial and radial stiffness produced by the HTS bearing, the vibration of the rotor is inevitable. The resonant points of the rotor were designed to be about 800 rpm and 13,000 rpm. We took the steady-state speed of 3000 rpm as an example to study the vibration of the rotor. During the rotor spinning steadily at 3000 rpm, in an arbitrarily selected time of 0.5 s, its fluctuation range of the displacement is −0.15 mm to 0.17 mm in the x-direction and −0.35 mm to 0.35 mm in the y-direction (see Fig. 10). They are both in the range of 0.4 mm and the vibration in the y-direction is more obvious. The radial displacement sometimes increases abruptly due to the torque ripple of the motor. Besides, the imbalance of the flywheel body (including its static and dynamic imbalance), as well as poor concentricity between the rotor and motor shaft, can cause the vibration of the rotor. Below the resonant frequency, the vibration in the x- and y-directions increases significantly with the speed, probably causing that the friction force between the shaft of the rotor and the protection bearing is produced and gradually increases. This is one of the reasons that the speed of the rotor cannot continue to rise [15]. So increasing the radial stiffness of the HTS bearing system (including the HTS bearings, PM bearings and AMBs, or including one or two types of them) to limit the radial vibration amplitude of the rotor is an effective way to improve the speed.

4 Conclusions

In this paper, we have built a small SFESS with a radial-type HTS bearing and an external motor. Its levitation characteristics were discussed and electromagnetic characteristics were studied by a mathematical model established based on the FEM. The analysis of the electromagnetic behaviors shows that lots of the magnetic field lines are limited in two kinds of small gaps: one is between the PMR and SMS, and the other is between every two adjacent HTS bulks. The induced current in the HTS bulks mainly distributes in their edges. So the larger electromagnetic force acts on the edge parts of the HTS bulks, probably leading to the crack for

the corresponding parts. This could have greater effect on the outer-rotor-type HTS bearing. We showed the free rotation curves of the rotor with different steady-state speeds of 2500–5000 rpm and analyzed its rotational characteristics. We measured the radial displacement of the rotor and think the vibration is closely related to the rotational characteristics, which is one of the reasons that the speed of the rotor cannot continue to rise. Limiting the vibration amplitude of the rotor is an effective approach to improve the speed and mechanical stability. Next, we are going to systematically study other characteristics of the prototype and design a large-scale SFESS, and the results will be reported in the future.

References

1. Han, H.S., Kim, D.S.: Superconducting magnet. In: Han, H.S., Kim, D.S. (eds.) Magnetic Levitation, pp. 51–74. Springer, Netherlands (2016)
2. Faraji, F., Majazi, A., Al-Haddad, K.: A comprehensive review of flywheel energy storage system technology. Renew. Sustain. Energy Rev. **67**, 477–490 (2017)
3. Strasik, M., Hull, J.R., Mittleider, J.A., Gonder, J.F., Johnson, P.E., McCrary, K.E., McIver, C.R.: An overview of Boeing flywheel energy storage systems with high-temperature superconducting bearings. Supercond. Sci. Technol. **23**, 034021 (2010)
4. Werfel Frank, N., Uta, F.-D., Rothfeld, R., Riedel, T., Goebel, B., Wippich, D., Schirrmeister, P.: Superconductor bearings, flywheels and transportation. Supercond. Sci. Technol. **25**, 014007 (2012)
5. Mukoyama, S., Nakao, K., Sakamoto, H., Matsuoka, T., Nagashima, K., Ogata, M., Yamashita, T., Miyazaki, Y., Miyazaki, K., Maeda, T., Shimizu, H.: Development of superconducting magnetic bearing for 300 kW flywheel energy storage system. IEEE Trans. Appl. Supercond. **27**(4), 3600804 (2017)
6. Ma, G.T., Liu, H.F., Wang, J.S., Wang, S.Y., Li, X.C.: 3D modeling permanent magnet guideway for high temperature superconducting maglev vehicle application. J. Supercond. Nov. Magn. **22**(8), 841 (2009)
7. Yu, Z.Q., Zhang, G.M., Qiu, Q.Q., Hu, L., Zhang, W.F., Zhuang, B.: Development status of magnetic levitation flywheel energy storage system based on high-temperature superconductor. Trans. China Electrotech. Soc. **28**(12), 109–118 (2013)
8. Koshizuka, N.: R&D of superconducting bearing technologies for flywheel energy storage systems. Phys. C **445**, 103–1108 (2006)
9. Han, Y.H., Park, B.J., Jung, S.Y., Han, S.C., Lee, W.R., Bae, Y.C.: The improved damping of superconductor bearings for 35kWh superconductor flywheel energy storage system. Phys. C **485**, 102–106 (2013)
10. Arsénio, A.J., Cardeira, C., Melício, R., Branco, P.J.C.: Experimental setup and efficiency evaluation of zero-field-cooled (ZFC)

YBCO magnetic bearings. IEEE Trans. Appl. Supercond. **27**(4), 1–5 (2017)

11. Hekmati, A., Hekmati, R., Siamaki, M.: Proposed design for superconducting magnetic bearing system with high-temperature superconducting discs. IEEE Trans. Appl. Supercond **27**(8), 1–8 (2017)

12. Naseh, M., Heydari, H.: Sensitivity analysis of rotor parameters in axially magnetized radial HTS magnetic bearings using an analytical method. IEEE Trans. Appl. Supercond. **26**(8), 1–11 (2016)

13. Sotelo, G.G., Rodriguez, E., Costa, F.S., Oliveira, J.G., de Santiago, J., Stephan, R.M.: Tests with a hybrid bearing for a flywheel energy storage system. Supercond. Sci. Technol. **29**(9), 095016 (2016)

14. Basaran, S., Sivrioglu, S.: Radial stiffness improvement of a flywheel system using multi-surface superconducting levitation. Supercond. Sci. Technol. **30**(3), 035008 (2017)

15. Fang, J.R., Lin, L.Z., Yan, L.G., Xiao, L.Y.: A new flywheel energy storage system using hybrid superconducting magnetic bearings. IEEE Trans. Appl. Supercond. **11**(1), 1657–1660 (2001)

16. Yu, Z.Q., Zhang, G.M., Qiu, Q.Q., Hu, L., Zhuang, B., Qiu, M.: Analyses and tests of HTS bearing for flywheel energy system. IEEE Trans. Appl. Supercond. **24**(3), 1–5 (2014)

17. Yu, Z.Q., Zhang, G.M., Qiu, Q.Q., Hu, L., Zhang, D., Qiu, M.: Analysis of levitation characteristics of a radial-type high-temperature superconducting bearing based on numerical simulation. IEEE Trans. Appl. Supercond. **25**(3), 1–5 (2015)

18. Hekmati, A., Hosseini, M., Vakilian, M., Fardmanesh, M.: A novel method of flat YBCO rings development for shield-type superconducting fault current limiters fabrication. Phys. C **472**(1), 39–43 (2012)

19. Sotelo, G.G., de Andrade, R., Ferreira, A.C.: Test and simulation of superconducting magnetic bearings. IEEE Trans. Appl. Supercond. **19**(3), 2083–2086 (2009)

20. Ma, G., Lin, Q., Jiang, D., Yuan, C., Deng, Z.: Numerical studies of axial and radial magnetic forces between high temperature superconductors and a magnetic rotor. J. Low Temp. Phys. **172**(3-4), 299–309 (2013)

21. Lu, Y., Wang, J., Wang, S., Zheng, J.: 3D-modeling numerical solutions of electromagnetic behavior of HTSC bulk above permanent magnetic guideway. J. Supercond. Nov. Magn. **21**, 467–472 (2008)

22. Zhou, P.B., Ma, G.T., Liu, H., Yang, C., Wang, Z.T., Gong, T.Y.: Experimental and numerical studies of the magnetic field transfer of a magnetic cylinder coated with superconductor. J. Supercond. Nov. Magn. **29**(7), 1747–1753 (2016)